THE JOURNAL OF PHYSICAL CHEMISTRY C

Article

pubs.acs.org/JPCC

On the Electrochemical Response of Porous Functionalized Graphene Electrodes

Christian Punckt,[†,‡] Michael A. Pope,[‡] and Ilhan A. Aksay*[,†]

[†]Department of Chemical and Biological Engineering, Princeton University, Princeton, New Jersey 08544, United States

[‡]Vorbeck Princeton Research Center, Vorbeck Materials Corp., 11 Deerpark Drive #203, Monmouth Junction, New Jersey 08852, United States

ABSTRACT: Electrodes used in electroanalysis, which are based on carbonaceous nanomaterials such as carbon nanotubes or graphene, often exhibit large degrees of porosity. By systematically varying the morphology of functionalized graphene electrodes from nearly flat to highly porous, we demonstrate experimentally that minute amounts of electrode porosity have surprisingly significant effects on the apparent reaction kinetics as determined by cyclic voltammetry, both in the reversible and the irreversible regime. We quantify electrode porosity using a coulometric approach and, with the help of numerical simulations, determine the correlation between electrode pore volume and apparent electrode kinetics. We show that in the reversible and quasi-reversible regime, the voltamperometric response constitutes a superposition of thin film diffusion-related effects within the porous electrode and of the standard flat electrode response. For irreversible kinetics, however, we show that diffusive coupling between the electrode and the electrolyte can, under suitably chosen conditions, result in effective electrocatalytic behavior. Confirming past theoretical work by Compton and others, our experiments demonstrate that for a comparison of electroanalytical data obtained with different electrode materials it is not sufficient to only consider differences in the materials' chemical structure but equally important to take into account differences in electrode morphology.

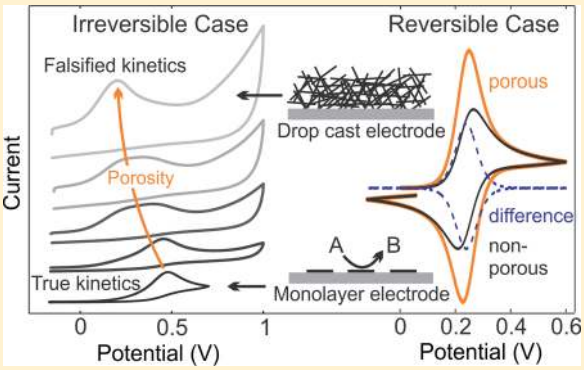

1. INTRODUCTION

Porous electrodes are used in numerous areas of electrochemistry:[1,2] The most prominent examples include electrical energy storage devices such as batteries[3−5] and energy conversion devices such as fuel cells[6−8] or dye-sensitized solar cells,[9−12] where porosity enables the diffusive or convective transport of electroactive species within the electrode, thus providing high surface area per unit volume (or mass) of the electrodes and increasing the rates of electron transfer reactions. The impact of electrode porosity in these energy-related systems has been studied in great detail both experimentally[8,13−15] and theoretically.[3,16−18]

Nonetheless, studies with porous electrodes conducted in the field of electroanalysis (e.g., electrochemical sensing and biosensing) typically neglect electrode porosity, although it is known to have a significant impact on effective kinetics of electrochemical reactions. With the advent of electrochemical sensing and biosensing based on carbonaceous electrode nanomaterials such as carbon nanotubes (CNTs)[19−21] and graphene,[22,23] this issue has become more pressing as these materials are typically used in the form of electrode films cast from a suspension onto flat substrates, a procedure that results in high surface area, porous structures.

The use of such CNT and graphene electrodes has led to an overwhelming number of scientific studies pointing out the benefits of these materials for electroanalysis and electrochemical sensors and biosensors for which we can only give a superficial account by referring the reader to recent review papers.[19,22−24] Because of the good performance of these new electrode materials, practically relevant parameters such as detection limits, sensitivity, and electrode stability could be significantly improved.[24,25] However, the impact of electrode morphology in evaluation and comparison of the electrocatalytic activity of CNTs and graphene is not considered. Instead, the reported electrocatalytic properties are commonly attributed solely to differences in the density of electroactive functional groups and defects decorating these materials, i.e., improvements in kinetic constants or reductions in overpotential determined from electrochemical data are thought to be caused only by the material chemistry.[22,23,26] Efforts have therefore been made to improve electroactivity by increasing the number density of defects and functional groups through activation procedures such as acid treatment for CNTs.[21] Similarly, the most reactive graphene electrodes have been obtained using functionalized graphene sheets (FGSs), which are produced through the graphite oxide (GO) route, either by

Received: May 24, 2013
Revised: July 8, 2013
Published: July 9, 2013

chemical reduction of graphene oxide (i.e., reduction of suspended individual layers of graphene oxide)[27] or thermal exfoliation and simultaneous reduction of GO.[28,29] The latter process yields a material with a high number density of oxygen-containing functional groups (both along the edges and on the surface of the sheets) and lattice defects,[28−30] which are thought to give rise to strong electrocatalytic effects.[5,12,22,31−34]

Already in 1997, however, theoretical studies by Zuo et al.[35] on roughness effects on electrode kinetics and detailed theoretical and experimental work in 2008 by Compton's group[36−38] on the impact of electrode porosity on cyclic voltammetry have shown that porous electrodes exhibit faster apparent kinetics with a given reactant than their flat equivalents. In other words, the kinetic constants extracted from data obtained with porous electrodes are determined not only by the intrinsic surface properties of the electrode material (i.e., functionalization and defectiveness) but also by electrode morphology. Consequently, in a more recent experimental study, Keeley and Lyons have pointed out that with single-walled CNT-modified electrodes, standard electrochemical tests that are interpreted based on the assumption of flat electrodes subjected to semi-infinite linear diffusion may lead to incorrect results.[39] Further, we have recently shown (by comparing FGS- and carbon black-modified glassy carbon (GC) electrodes for the oxidation of nicotinamid adenine dinucleotide (NADH)) that the porosity of the electrodes contributes to apparent electrocatalytic effects.[33] In order to measure the deviation of the porous electrode response from ideal flat behavior, we have introduced a phenomenological porosity factor and showed that the apparent kinetics of electrochemical reactions were correlated with this porosity factor and were thus related to electrode morphology.[33]

However, in all previous electroanalytical studies with FGS-based electrodes or other carbonaceous nanomaterials, no in situ quantification of electrode porosity was conducted and no benchmark performance was obtained in the complete absence of porosity. Consequently, experimental studies in which the electrode porosity was systematically varied from flat to highly porous (to show the impact of electrode morphology on apparent electrode kinetics without varying the intrinsic nature of the electrode material) are not available in the literature.

Here, we present experiments in which we systematically vary the porosity of FGS electrodes and quantitatively analyze its impact on the response toward two standard redox probes, ferrocyanide (FC) and NADH, the former exhibiting quasi-reversible and the latter irreversible kinetics. By comparing the results obtained with porous drop-cast FGS electrodes on GC substrates with those obtained using FGS monolayer (ML) electrodes, which exhibit the smallest degree of porosity that can be achieved with this material,[40] we demonstrate that in the case of (quasi-) reversible kinetics, the porous electrode response can be used to characterize cumulative pore volume and pore size and that these parameters dominate the apparent kinetics obtained with an irreversible redox reaction. We further show that FGSs intrinsically only exhibit a negligible increase in electroactivity toward FC and NADH compared to GC but that minute amounts of electrode porosity or roughness are sufficient to cause significantly faster apparent electrode kinetics. Our experimental work is accompanied by numerical simulations to elucidate the contribution of ion transport in the bulk electrolyte and within the porous electrode film to the overall electrochemical response.

2. METHODS

2.1. FGS Processing. GO was prepared in a modified Hummers process described elsewhere.[41] To obtain FGSs, about 200 mg of GO was placed in a fused silica tube and dried overnight under a flow of argon gas. The tube was then evacuated and inserted into a furnace where it was exposed to a temperature of 1100 °C for 60 s. After removal of the tube from the furnace, the material was allowed to cool to room temperature. Its degree of reduction was determined by energy dispersive X-ray spectroscopy (INCA x-act, Oxford Instruments, UK attached to a Vega 1 scanning electron microscope (SEM), Tescan USA), which yielded a carbon-to-oxygen ratio (C/O) of about 20.

2.2. Electrode Fabrication. FGSs were suspended in 1,2-dichloroethane (DCE) at a concentration of 0.1 mg/mL using tip sonication (Vibracell, Sonics & Materials Inc., CT). Various amounts of suspension were then drop-cast onto freshly polished square GC substrates with 1 cm^2 surface area at a substrate temperature of 80 °C (to accelerate solvent evaporation), such that electrodes with FGS loadings between 5 and 200 $\mu g/cm^2$ were obtained. SEM images of FGSs coated according to this procedure onto 1 cm^2 pieces of a Si(100) wafer (allowing for substrate cleaving and subsequent imaging of the cross-section) are shown in Figure 1a−c.

For the fabrication of FGS MLs, we coated highly oriented pyrolytic graphite (HOPG) and flame-annealed gold substrates with the help of a Langmuir−Blodgett (LB) trough, as detailed elsewhere.[40] In short, a suspension of FGSs in DCE at a concentration of 0.1 mg/mL was prepared by tip sonication and dripped onto the deionized (DI) water that filled the LB trough. Because of the spreading of the DCE on the air/water interface, a thin film of FGSs formed that was subsequently compressed with the use of two movable Teflon barriers such that the FGSs were packed densely at the air/water interface but did not overlap.[40] HOPG and gold substrates were placed beneath the FGS film, and the water level was lowered, so that the FGS film was transferred onto the substrates. Coated HOPG and gold substrates were then dried at ∼200 °C overnight. Figure 1d,e shows SEM and atomic force microscopy (AFM) images of an FGS ML on gold illustrating dense packing as well as the presence of microscopic wrinkles and folds present in the FGS film. To block the electrochemical response of the gold substrates, the FGS-coated samples were placed in a 1 mM solution of hexadecanethiol in ethanol for 4 h before use.[40]

2.3. Electrochemical Characterization. Electrochemical measurements were conducted using a custom-made polytetrafluoro-ethylene (PTFE, Teflon) cell shown schematically in Figure 1f.[40] FGS-coated GC, HOPG, or gold substrates served as working electrode (WE). A platinum mesh was used as a counter electrode (CE), and the potential was measured with a Ag/AgCl reference electrode (RE) whose tip was located 3−4 mm above the working electrode. All potentials in this work are reported versus a Ag/AgCl (1 M KCl) reference. The ferro/ferricyanide (FC) redox couple was used to explore electrode responses in the quasi-reversible regime. Ferrocyanide was dissolved at a concentration of 2.5 mM in 0.1 M phosphate-buffered saline (PBS) at pH 7.4, and KCl was added to obtain a final KCl concentration of 1 M to minimize Ohmic drops in the electrolyte. Separately, PBS background electrolyte with 1 M total KCl concentration was prepared to conduct background measurements in the supporting electrolyte alone. NADH was

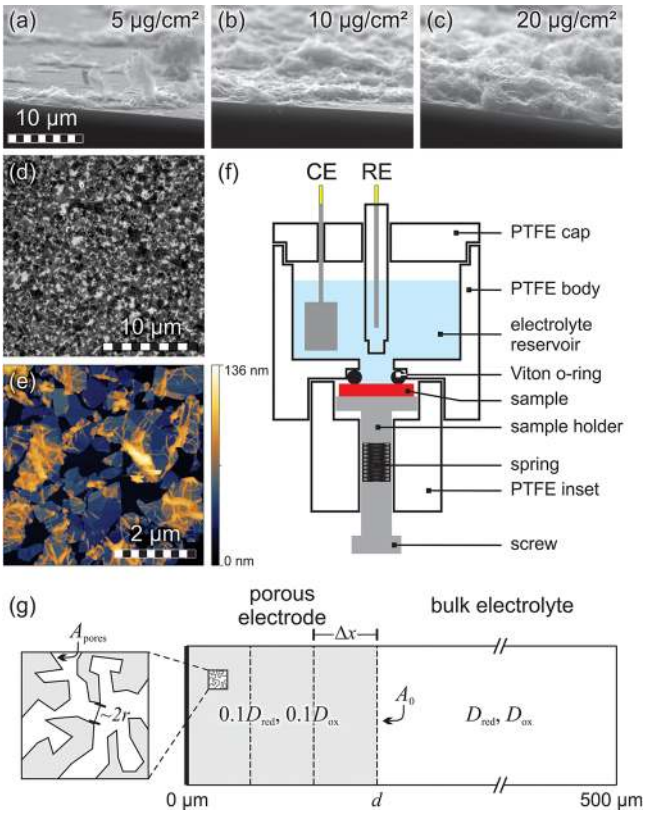

Figure 1. (a–c) SEM images of drop-cast FGS films with indicated FGS loading. At 5 $\mu g/cm^2$, the FGSs are aggregated in sparsely distributed clusters, leaving a substantial part of the electrode surface uncovered. At higher loadings, the FGS film becomes more homogeneous, reaching a thickness on the order of 5 μm at 20 $\mu g/cm^2$. All films visually appear rough and porous. (d) SEM image of an FGS ML on a gold substrate. FGSs appear dark on a bright gold background. (e) AFM image of FGS ML on HOPG. The sheets are densely tiled and exhibit the typical wrinkles and folds observed previously.[37] (f) Schematic of the electrochemical cell. (g) Illustration of system layout for numerical simulations with porous electrodes. Dashed lines represent the spatial discretization within the electrode during simulation. The characteristic pore size r (see magnified view on the left) is not spatially resolved and therefore not directly considered in the simulations. Instead, spatially averaged effective transport and kinetics are evaluated as detailed in the text.

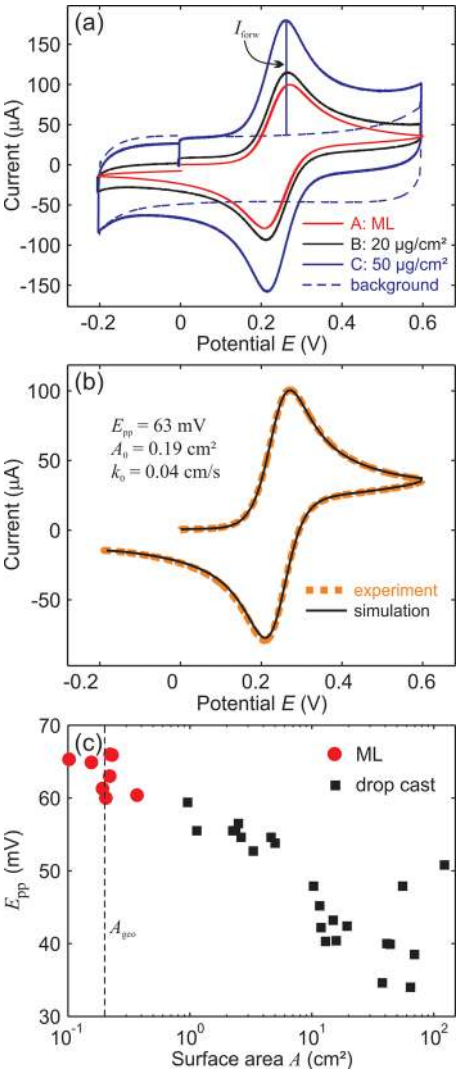

Figure 2. Experimental results obtained with the FC redox probe. (a) Comparison of CVs obtained with a ML electrode (on passivated gold) and drop-cast electrodes with indicated FGS loading. The dashed gray line represents the separately measured capacitive background current for electrode C (50 $\mu g/cm^2$). (b) CV from ML electrode shown in panel a overlaid with a fitted computer-generated CV using our in-house simulation code. (c) E_{pp} as a function of electrolyte-accessible surface area determined through PEIS. The dashed vertical line indicates the average geometric surface area determined from ML electrodes using electron and optical microscopy.

employed to analyze electrode responses in the irreversible regime, using a 2.5 mM solution of NADH in 0.1 M PBS (pH 7.4) without further addition of KCl.

Experiments were conducted at room temperature with a computer-controlled potentiostat (Model VSP, Biologic USA) using forward feedback to correct for 85% of the Ohmic drop (typically 30–50 Ω) determined by an impedance measurement at 50 kHz, 20 mV amplitude, and open circuit voltage (OCV) prior to electrochemical testing. After Ohmic drop correction, with each electrode, first a series of cyclic voltammograms (CVs) at scan rates υ between 50 and 2000 mV/s were recorded in background electrolyte in a potential window ranging from −200 to +600 mV to obtain the capacitive background current (see dashed line in Figure 2a). Starting potential was 0 mV. This was followed by potentiostatic electrochemical impedance spectroscopy (PEIS) at a potential of 240 mV in the range from 500 to 0.001 kHz to determine the electrode capacitance. Then, the electrolyte was exchanged with the FC-containing solution, and CVs were recorded within the same potential window and at the same scan rates as used for the background measurements. The electrolyte was then removed, and the cell was rinsed at least 6 times with DI water to ensure that no significant amount of FC was left behind. In particular for the FGS films with the largest loading, this procedure had to be performed carefully and slowly to avoid rinsing off parts of the electrode film and to allow for residual FC to diffuse out of the electrode films. The electrodes were then used to oxidize NADH by recording a CV scan from OCV to 1000 mV and back to the OCV at a scan rate of 100 mV/s. For FGS MLs on thiol-passivated gold, a maximum potential of 650 mV was chosen in order to not compromise the passivation layer.[40] Finally, ML electrodes were imaged with SEM, optical microscopy (Axioplan 2 with AxioCam HRc, Carl Zeiss MicroImaging Inc.), and contact

dx.doi.org/10.1021/jp405142k | J. Phys. Chem. C 2013, 117, 16076–16086

mode AFM (Veeco Multimode with Nanoscope IIIa controller). SEM and optical microscopy images were used to determine the geometric surface area A_{geo} of the section of the WE that was exposed to the electrolyte. This was done by measuring the diameter of the imprint of the O-ring used to seal the WE against the PTFE body left on the electrode. We obtained an average value of $A_{geo} \approx 0.22$ cm^2.

2.4. Numerical Simulations. CVs were simulated using a code written in-house in MatLab to allow for versatile interfacing with experimental voltammetry data (see below). All simulations were performed in one spatial dimension using a system size of 500 μm, a spatial resolution of $\Delta x = 1$ μm (500 points), a time step of 10^{-7} s, and no-flux boundary conditions using Euler integration, unless noted otherwise. Reaction kinetics were defined by the Butler–Volmer equation:[42]

$$I = nFA_0k_0\left(C_{red}\exp\left\{\frac{nF\tilde{E}}{RT}\right\} - C_{ox}\exp\left\{\frac{-nF\tilde{E}}{RT}\right\}\right) \quad (1)$$

Here, I denotes the net redox current, n is the number of electrons involved in the reaction, F is the Faraday constant, A_0 is the projected electrolyte-accessible surface area (in theory, $A_0 = A_{geo}$), k_0 is the rate of heterogeneous electron transfer, C_{red} and C_{ox} are the concentrations of reduced and oxidized redox species at the electrode/electrolyte interface, $\tilde{E} = E - E_0$ is the overpotential, i.e., the difference between applied potential E and equilibrium potential E_0, R is the universal gas constant, and T is the absolute temperature (298.15 K). We assumed 1-dimensional linear diffusion of reduced and oxidized species with diffusion coefficients of $D_{red} = 6.3 \times 10^{-5}$ cm^2/s and $D_{ox} = 7.6 \times 10^{-5}$ cm^2/s, which resemble the transport of the FC redox probe.[42] The simulations were initialized by setting the concentrations of the reduced and the oxidized species to values of 2.5 and 0 mM, respectively.

The accuracy of our simulation code was extensively tested by calculating CVs in a wide range of kinetic regimes and comparing the results such as peak-to-peak separation $E_{pp} = E_{forw} - E_{rev}$ (i.e., the separation between the locations of the oxidation (forward) and reduction (reverse) peak on the potential axis) and peak oxidation current I_0 either with analytically obtained values[42] or with numerical data published in the literature,[42] yielding excellent agreement.

CVs for porous electrodes were calculated in one spatial dimension as well, using a phenomenological approach outlined in the following and illustrated in Figure 1g. Effective ion flux within the porous electrode is decreased compared to transport through the bulk electrolyte due to resistance induced by the tortuosity and constriction effects of the porous medium. Modeling the transport of ionic species in porous materials in full detail, i.e., taking into account the actual pore structure and surface interaction effects, is a complex matter and has been the topic of numerous studies.[17,18,43,44] For the purpose of this study, however, it was sufficient to describe the porous film as a region of length (i.e., thickness) d in which the diffusive transport of the redox species is effectively hindered and only spatially averaged properties are considered.[16,45] Convective effects were neglected. We therefore described the transport within the porous film solely by reducing effective diffusion coefficients in that region, a strategy that has been used by Newman[16] and others.[46] We set the diffusion coefficients within the porous film to one tenth of their bulk values,[45] which proved to give results in qualitative agreement with our experiments.

Throughout the porous film, we assumed the same reaction kinetics as on a flat electrode (eq 1) and uniform electric potential, so that the only simulation variables varying within the porous film were C_{red} and C_{ox}. To calculate charge transfer rates within the porous film for a given characteristic pore size r, we assigned an effective electrochemically active surface area $A_{pores} = A_0\Delta x/r$ to each volume element Δx, which was thought to represent the cumulative surface area of all pores within Δx. In effect, this is analogous to assuming that the electrolyte contained within the pores of one volume element is spread out to a layer of thickness r and surface area A_{pores}. Thus, our simulation assumes slit-like pores of width r. The influence of r on effective diffusivity was not considered since we were not aiming for a realistic model but rather for a conceptual understanding of porosity effects.

2.5. Analysis of Experimental Data. For measurements with the FC redox couple, E_{pp} was determined from CVs obtained at $\nu = 100$ mV/s. For the determination of the peak oxidation (forward) current I_{forw}, the measured capacitive background current at E_{forw} was subtracted from the peak current obtained in the FC electrolyte (see example in Figure 2a).

CVs measured with the FC redox couple and FGS ML electrodes at a scan rate of typically 100 mV/s were fitted with simulated CVs in a multistep process in order to obtain k_0 and A_0: First, a value of k_0 was determined that resulted in the value of E_{pp} obtained from the measurement. This process was greatly accelerated by making use of a precalculated table that related E_{pp} to k_0 and using a spline interpolation method to determine values in between the tabulated ones. In a second step, a CV was calculated for the obtained value of k_0, using a starting value for the electrode surface area of $A_{start} = A_{geo}$ and a starting value for E_0 chosen as the average of experimental forward and reverse peak potentials. Since the resulting simulated CV did not contain any contributions from capacitive background current, we added the measured background CV to the simulated curve. This procedure often resulted in a slight mismatch between the calculated and the experimental value of I_{forw} and a shift of a few mV on the potential axis. This mismatch was minimized by shifting the simulated CV along the potential axis so that simulated and experimental values of E_{forw} and E_{rev} matched (resulting in a corrected value for E_0), and by multiplying the calculated redox current with a suitable correction factor a (from which we obtained a fitted surface area of $A_0 = aA_{start}$) such that simulated and experimental values of I_{forw} were in agreement.

The double layer capacitance C_{DL} of the FGSs used in this study was determined by PEIS with ML electrodes in background electrolyte as detailed recently.[40] We obtained an average value of $C_{DL} = 20$ μF/cm^2 at a frequency of $f = 100$ Hz and $E = 240$ mV. The total electrolyte-accessible surface area A of individual ML electrodes and drop-cast electrodes was determined by dividing their measured capacity C (as determined from electrode impedance Z at $f = 100$ Hz) by C_{DL}:

$$A = \frac{C}{C_{DL}} = \frac{1}{2\pi C_{DL} f\,\mathrm{Im}(Z)} \quad (2)$$

CVs obtained in experiments with drop-cast electrodes and FC electrolyte were processed by subtracting the sum of the measured background CV and a simulated flat electrode CV from the original voltammetry data in order to isolate the contribution of the pore space to the overall voltammetric response. The simulation parameters were chosen as follows.

We set k_0 = 0.05 cm/s, which corresponds to the average rate of electron transfer measured with ML electrodes in this work. For A_0 and E_0, we chose the same starting values as used for ML CV fitting described above. The resulting simulated curve was centered on the potential axis with respect to the experimental redox peaks to adjust for the deviation in E_0. The correction factor a was adjusted such that the oxidation currents were in agreement at E = 500 mV.

3. RESULTS AND DISCUSSION

3.1. Reversible and Quasi-Reversible Kinetics. Figure 2a shows CVs obtained with the FC redox couple using an FGS ML (electrode A) and two drop-cast electrodes with FGS loadings of 20 and 50 μg/cm^2 (electrodes B and C). All curves display the characteristic peaks related to the oxidation and subsequent reduction of the redox couple. For electrode A, the peak-to-peak separation is E_{pp} = 63 mV, and the oxidation peak current is I_{forw} = 99.7 μA. By fitting with a computer-generated CV (Figure 2b), taking into account reported values for the diffusion coefficients for ferro- and ferricyanide (D_{red} = 6.3 × 10^{-5} cm^2/s and D_{ox} = 7.6 × 10^{-5} cm^2/s),[42] we obtain an equilibrium potential of 239 mV, a heterogeneous rate constant of k_0 = 0.04 cm/s (quasi-reversible), and a projected electrode surface area of A_0 = 0.19 cm^2, which is in reasonable agreement with the total electrolyte-accessible surface area A = 0.22 cm^2 estimated from PEIS (eq 2) and the size of the imprint of the Viton O-ring A_{geo} ≈ 0.21 cm^2 determined by SEM. $A_0 < A_{geo}$ suggests that the O-ring covers a slightly larger area of the electrode than is evident from the imprint. We determined k_0 and A_0 for all ML electrodes tested in this study, obtaining average values of k_0 = (0.05 ± 0.02) cm/s and A_0 = (0.19 ± 0.02) cm^2.

Electrodes B and C exhibit peak-to-peak separations of 52.7 and 45.2 mV, respectively. For a Nernstian (reversible) one-electron redox reaction, E_{pp} ≈ 57 mV,[42] which constitutes the minimum value the peak to peak separation can attain on a flat electrode. Therefore, the CVs obtained with the drop-cast electrodes cannot be fitted, and kinetic constants cannot be determined, illustrating that in the case of drop-cast electrodes E_{pp} is not solely defined by the intrinsic reaction kinetics but, as expected, is also affected by electrode porosity. An analysis of the peak oxidation currents for electrodes B and C reveals that I_{forw} increases with increased FGS loading, yielding values of 105 μA (electrode B) and 128 μA (electrode C). Peak current, however, should in theory only depend on A_0, D_{red}, ν, and the bulk electrolyte concentration, which are in good approximation identical for electrodes A–C. The observed increase in I_{forw} with FGS loading thus further emphasizes significant deviation from the classical flat electrode behavior.

The results thus far resemble the characteristic changes in peak current and peak separation as a result of electrode porosity reported in the theoretical work by Menshykau and Compton[36] and observed (with different electrode materials) in our own recent study on NADH oxidation.[33] By analyzing CV data from our ensemble of FGS electrodes, we will, in the following, show how porosity effects can be quantified experimentally and related to intrinsic reaction kinetics by (i) measuring the electrolyte-accessible surface area, (ii) determining the dependence of peak current on scan rate, and (iii) subtracting simulated flat electrode CVs from data that is affected by electrode porosity.

The observed decrease in E_{pp} and the increase in I_{forw} in our data with increasing FGS loading are accompanied by a significant rise of the capacitive background current (shown in Figure 2a as dashed line for the 50 μg/cm^2 electrode) from I_{cap} = 1 μA in the case of the ML electrode to I_{cap} = 38 μA for the drop-cast electrode with 50 μg/cm^2. This is indicative of an increase in electrolyte-accessible surface area A.[42] To quantify the changes in A with varying FGS loading, we use EIS to measure the electrode capacitance because background currents obtained by cyclic voltammetry are to a small extent compromised by Faradaic contributions and uncompensated Ohmic drops. With EIS, we measure capacities of 4.4, 66, and 230 μF for electrodes A–C, and according to eq 2, the corresponding electrolyte-accessible surface areas are 0.22, 3.3, and 11.6 cm^2.

Figure 2c shows E_{pp} as a function of A for all electrodes tested in this study. We observe a clear trend of decreasing E_{pp} with increasing A, and E_{pp} reaches values as low as 34 mV. For the ML electrodes, values of A between about 0.10 and 0.37 cm^2 are measured, indicating that some MLs are not densely coating the electrode substrate ($A < A_{geo}$) and others are exhibiting a certain degree of roughness ($A > A_{geo}$), probably due to a higher degree of wrinkling and folding of the FGSs or due to the occurrence of FGS aggregates in the electrode coating which could not be completely eliminated during ML fabrication. For A > 20 cm^2, the scattering of E_{pp} is noticeably increased, and we occasionally observe values of E_{pp} around 50 mV, i.e., larger peak-to-peak separation than in the case of electrodes with smaller A. We attribute this to Ohmic drops within the thickest FGS coatings due to the tortuous path for both electrons through the FGS network and ions through the electrolyte-filled pores. Despite a substantial scatter in the data, A (or alternatively A/A_0) is a reasonable measure for electrode porosity, and in case data from flat electrodes were not available, the reaction kinetics could be approximated by extrapolation of data obtained with drop-cast electrodes to the point where $A = A_0$ if a sufficient amount of data obtained with electrodes of varying A is measured.

CVs recorded with electrodes A and C at various scan rates ν between 50 and 2000 mV/s are shown in Figure 3a,b. For a Nernstian system on a flat electrode with linear hemispherical diffusion, I_{forw} is proportional to the square root of ν,[42] thus $\alpha = I_{forw}/\sqrt{\nu}$ is constant. For electrodes A and C, we plot α as a function of ν in Figure 3c. In the case of the ML electrode A, α is approximately constant. The slight decrease in α by about 7% may be attributed to the fact that at the highest scan rates the system begins to transition toward the irreversible regime in which the peak current is reduced.[42] Another possible reason might be an incomplete coverage of the substrate with FGSs, which leads to effectively reduced electrode surface area at high scan rates and thus decreased redox current.[47]

For the drop-cast electrode C, we obtain a behavior that is qualitatively different from that of the ML and is characterized by a pronounced increase of α with ν. To quantify this deviation from the flat electrode behavior, we have previously introduced a porosity factor P defined as the ratio of the scan rate-normalized peak currents at maximum and minimum scan rate:[33]

$$P = \frac{\alpha(2000\ \text{mV/s})}{\alpha(50\ \text{mV/s})} \tag{3}$$

For a Nernstian system on a flat electrode with linear hemispherical diffusion, P = 1. E_{pp} as a function of P is plotted in Figure 3d showing that the deviation of the peak currents is a

dx.doi.org/10.1021/jp405142k | J. Phys. Chem. C 2013, 117, 16076–16086

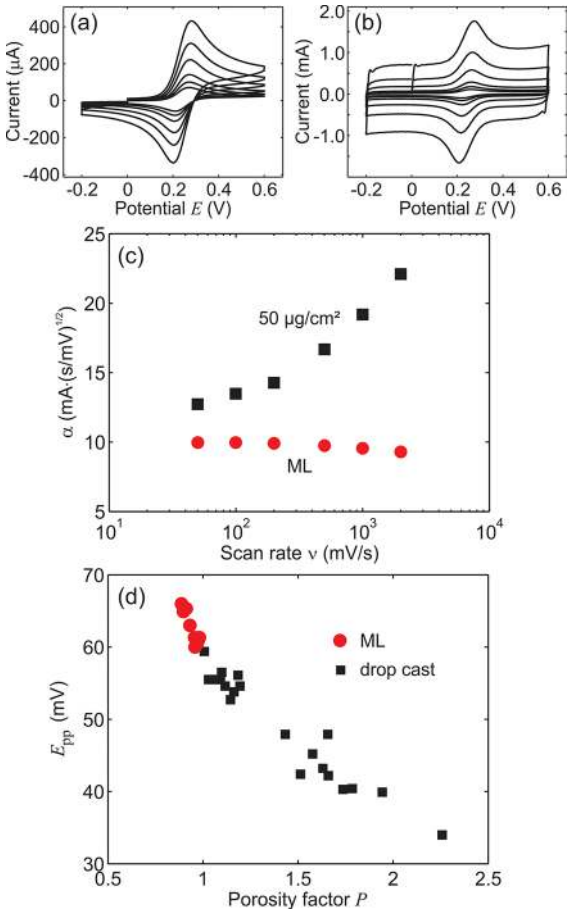

Figure 3. Analysis of scan rate behavior using the FC redox probe. CVs obtained with ML (a) and drop-cast (b) electrode at scan rates of 50, 100, 200, 500, 1000, and 2000 mV/s. (c) Change in the scan rate behavior of I_{forw} as expressed by variations in α. (d) Porosity factor[33] and corresponding peak-to-peak separation determined from all measurements conducted in this study.

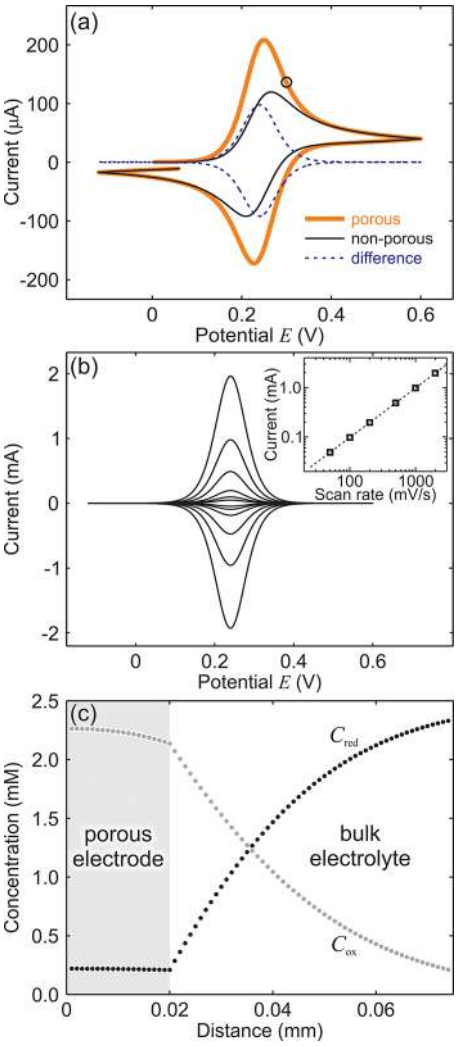

Figure 4. Numerical simulations for quasi-reversible electrode kinetics: k_0 = 0.05 cm/s, E_0 = 240 mV, and A_0 = 0.22 cm^2. (a) Comparison of CVs simulated for a porous electrode with d = 20 μm and a flat electrode. The blue dashed line represents the difference between the two. The black circle indicates the point for the concentration profile shown below. (b) Scan rate dependence of the difference between porous and flat electrode CVs showing linear dependence of the magnitude of the difference (inset). (c) Concentration profile within and near the porous electrode whose CV is presented in (a) at a potential of 300 mV (black circle in panel a).

more sensitive measure of the effects of electrode morphology than A. Even among the ML electrodes, a clear trend in decreasing E_{pp} with increasing P is seen, which means that even though ML electrodes resemble a flat electrode more closely than any drop-cast electrode, effects of electrode morphology are still present and impact the apparent electrode kinetics. Because of the small scatter in the data, extrapolation of data obtained with porous electrodes with $P > 1$ to a value of $P \approx 0.9$ (for fully reversible kinetics, $P = 1$) can be used to determine the true electrode kinetics if a sufficiently wide range of values of P is covered experimentally.

Both A and P are indirect measures of electrode porosity. In the following, we show that, by combining simulations with experimental data, we can extract the cumulative pore volume V and the approximate characteristic pore size r from our measurements with drop-cast electrodes. To this end, we first use a phenomenological approach to simulate electrode porosity as outlined in the Methods section where also most of the simulation parameters are specified.

Figure 4a displays the result of a CV simulation for which we chose an electrode with thickness d = 20 μm and a pore size of r = 50 nm, in comparison to a CV simulated for a flat electrode. As expected, we find that the porous electrode exhibits both a smaller value of E_{pp} (22.3 mV) and increased I_{forw} (208 μA) compared to the flat electrode (61.5 mV and 117 μA). After subtracting the CVs of porous and flat electrode (dashed line in Figure 4a), we obtain a pair of peaks, each of which is centered around the equilibrium potential and whose magnitudes depend linearly on scan rate (Figure 4b). These are the typical characteristics of a redox system under thin-film diffusion conditions.[42] Therefore, in the case of fast electrode kinetics, it appears that the CV obtained with a porous electrode is – at least in good approximation (as explained below) – the sum of a semi-infinite diffusion response of the electrode/bulk electrolyte interface and a thin-film response originating from the electrolyte within the porous electrode.

This can be more easily understood by considering the changes in electrolyte concentration both within and outside the porous electrode, as illustrated in Figure 4c. In the given case of nearly Nernstian kinetics (k_0 = 0.04 cm/s, ν = 100 mV/s), the concentration of the reduced species C_{red} within the electrode during the forward sweep is in good approximation a

dx.doi.org/10.1021/jp405142k | J. Phys. Chem. C 2013, 117, 16076–16086

function of only the instantaneous value of the potential and therefore is not a function of space. As a result, the magnitude of the diffusive transport of the reduced species from the bulk electrolyte into the porous electrode is negligible, and during the forward sweep C_{red} at the electrode/bulk electrolyte interface is approximately the same as in the flat electrode case. Thus, the thin-film diffusion part of the CV is the result of the depletion of the reduced species contained in the electrode pores, while the processes in the bulk electrolyte are in good approximation identical to those on a flat electrode with semi-infinite linear diffusion. Consequently, once the pore space is depleted during the forward scan at $E > \sim 400$ mV, the porous electrode CV coincides with that of the flat electrode: Only at the electrode/bulk electrolyte interface, the reduced electrolyte species are available, and the porous electrode effectively behaves like a flat one since the oxidation current is governed by diffusive transport of the redox molecule through the bulk electrolyte.

However, these considerations are only approximately accurate since the oxidized species generated during the forward sweep diffuses from the porous electrode into the bulk, as can be seen from the drop in C_{ox} within the porous film near the bulk electrolyte. This has an impact on the net current and therefore constitutes a deviation from the ideal case of full independence between processes inside the porous film and in the bulk electrolyte. Nonetheless, the linearity of the extracted thin-film-like response (Figure 4b inset) shows that this deviation is negligible for the parameters chosen. The diffusive coupling between the processes within the porous electrode and at the electrode/bulk electrolyte interface becomes stronger with slower reaction kinetics and decreasing difference between D_P and D_0. The former case will be seen in the analysis of irreversible kinetics below.

We will now use the possibility to decouple the processes within and on the surface of porous electrodes to analyze electrode porosity in our experimental data in more detail. To this end, we generate a simulated flat electrode CV based on parameters extracted from our ML electrode experiments and subtract this simulated response as well as the experimentally determined capacitive background current from the original porous electrode CV (Figure 5a). (Details of this procedure are given in the Methods Section.) The result is a pair of peaks (dashed line in Figure 5a) that exhibits nearly linear scan rate dependence (Figure 5b,c), i.e., that exhibits the characteristics of a response due to thin-film diffusion,[42] analogous to our simulation results (Figure 4). We conclude that our experimental conditions are suitable to assume that only negligible diffusive transport from the bulk into the porous film occurs during recording of the CVs and that the redox currents generated within the porous electrode and at the electrode/bulk electrolyte interface can be separated in good approximation. For electrodes with small FGS loading (<10 μg/cm^2), however, we found that this assumption only holds at scan rates >200 mV/s. At smaller scan rates, diffusive transport between the porous electrodes and the bulk electrolyte resulted in inflated current values. For small FGS loading, we therefore conducted our subtraction analysis with CVs measured at 500 mV/s.

The amount of charge represented by the thin-film peaks shown in Figure 5b is about 41 μC. The oxidation reaction associated with the transfer of this charge from the electrolyte to the electrode leads to the complete depletion of ferrocyanide within the pores. Therefore, according to Faraday's law, in the

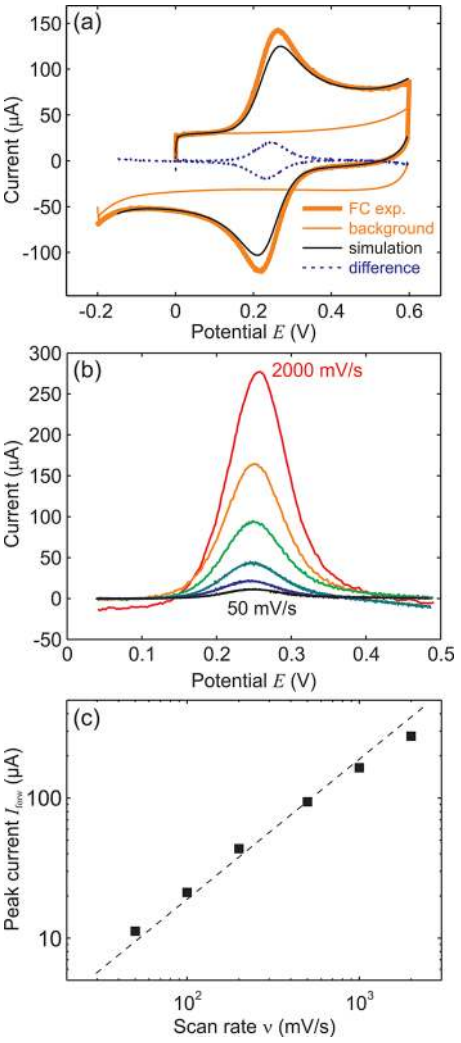

Figure 5. (a) Processing of experimental CV obtained with electrode C and FC at 100 mV/s(thick orange line). The black line represents the sum of computer-generated CV (not shown) and measured capacitive background current (dash-dotted orange line). The difference between experimental and simulated curve is shown as a dashed blue line. (b) Difference between experimental and simulated forward peak as a function of scan rate. (c) Double-logarithmic plot of the scan rate dependence of the peak currents seen in panel b. The dashed line represents a linear fit of the data, which apparently shows a slight deviation from ideal linear behavior.

shown example, the pores were filled with a total of 4.2×10^{-10} moles of ferrocyanide. Given the electrolyte concentration of 2.5 mM, we calculate a pore volume of $V = 4.2 \times 10^{-10}$ mol/2.5 mM = 0.169 μL. The average thickness of the electrode can be approximated by dividing V by A_0 (0.22 cm^2), which gives a value of d = 7.7 μm. (The contribution of FGSs to the film thickness is negligible and lies on the order of 200 nm.) An approximation of the characteristic pore size can be obtained by dividing V by A (11.6 cm^2, determined through PEIS), yielding $r \approx 0.17\ \mu$L/11.6 cm^2 = 0.15 μm. This approximation assumes slit-like parallel pores, which is certainly not a realistic assumption but suffices to provide the order of magnitude of r.

The above analysis has been conducted for all measured electrodes with the exception of most FGS MLs, for which no pore volumes or related parameters could be extracted due to limitations in the accuracy of the method, and for which we therefore set V = 0 μL. Only for three ML electrodes, a

dx.doi.org/10.1021/jp405142k | J. Phys. Chem. C 2013, 117, 16076−16086

significant deviation from the simulation was detected, and for these electrodes, pore volumes are reported, which range from 3 to 6 nL. We attribute the occurrence of porosity to the presence of FGS aggregates, which are also occasionally observed as several micrometer diameter agglomerates by SEM and are likely due to an incomplete separation of FGSs into individual sheets during suspension preparation prior to ML fabrication. Figure 6a shows E_{pp} as a function of V. We

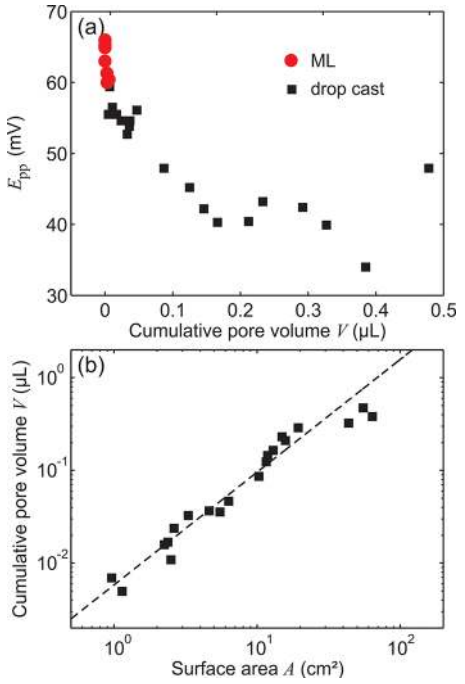

Figure 6. (a) Peak-to-peak separation obtained with FC at 100 mV/s plotted as a function of cumulative pore volume for all electrodes tested. (b) Cumulative pore volume as a function of electrolyte-accessible surface area. The dashed line represents a power law fit to the data.

observe a similar trend as seen in Figure 3d. However, for $V >$ ~0.2 μL, E_{pp} is found to level off and finally increase slightly with increasing V. This is probably the consequence of Ohmic drops within the thick (15–25 μm) porous films associated with these electrodes, an effect that has been studied in detail by de Levi (distributed resistance).[48] Interestingly, a final increase in E_{pp} for the most porous films is not seen in the plot showing E_{pp} as a function of P (Figure 3d). In the presence of Ohmic drops, P is decreased while E_{pp} is increased, and the corresponding data point shifts along the curve to the top left of the diagram. Thus, a characterization of porosity based on P alone can be misleading. However, P shows greater sensitivity to the onset of porosity (i.e., to electrode roughness) than V and is therefore useful to assess the flatness of ML electrodes.

A plot of V as a function of A is shown in Figure 6b. The dashed line represents a fit to the data using the (unitless) equation $V = xA^y$ from which we obtain $x = 0.0059$ and $y = 1.2$. V is therefore a slightly nonlinear function of A and characteristic pore size in our electrodes depends on FGS loading: While for $A = A_0$, on the basis of the fit, an average characteristic pore size of $r = V/A = 43$ nm (again assuming slit-like parallel pores) is obtained, $A = 10$ cm^2 yields $r = 93$ nm. This increase in characteristic pore size with increasing FGS film thickness is likely due to differences in drying dynamics during coating of the GC substrate. As will be shown in the following, pore volume and pore size are key parameters in understanding CVs obtained with redox molecules that exhibit irreversible kinetics.

3.2. Irreversible Kinetics. Figure 7a shows CVs of NADH oxidation obtained with a GC electrode, an FGS ML electrode,

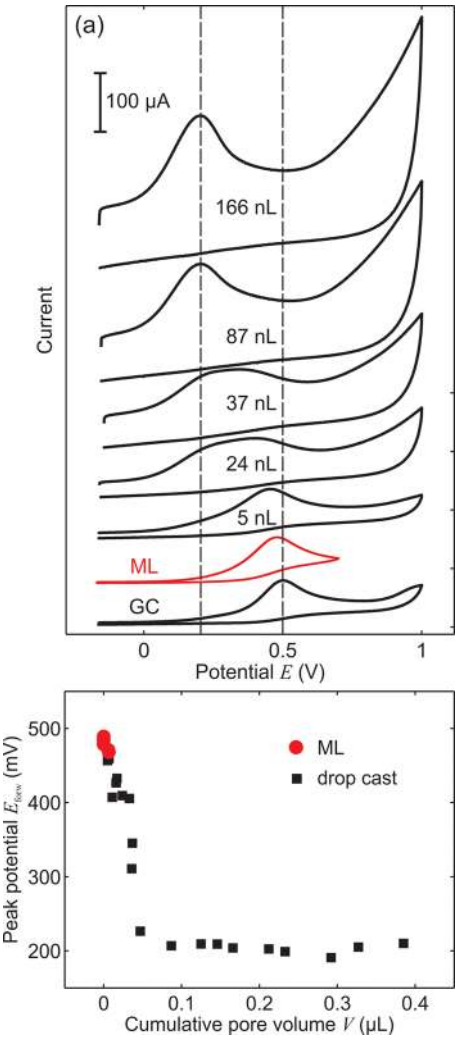

Figure 7. NADH oxidation experiments. (a) CVs obtained with various electrodes of different pore volume in comparison to the response obtained with a GC electrode. (b) Peak oxidation potential for NADH oxidation for all tested FGS electrodes.

and five drop-cast electrodes exhibiting different cumulative pore volumes (determined through FC oxidation as described above performed prior to NADH oxidation). The peak potential for NADH is 500 mV using the GC electrode. With the FGS ML, we measure 480 mV indicating that the FGS ML provides only little advantage compared to GC, which might be due to the onset of porosity (which in this case might be better referred to as electrode roughness) as seen for FC in Figure 3d. For the different drop-cast electrodes, we obtain smaller potentials down to 204 mV in the case of $V = 169$ nL (electrode C). Peak potentials for all measured electrodes as a function of V are shown in Figure 7b where we again assign $V = 0$ μL to all ML electrodes. This overview shows that up to a pore volume of about 0.1 μL the peak potential decreases sharply but then remains constant for $V > 0.1$ μL. Such peak

dx.doi.org/10.1021/jp405142k | J. Phys. Chem. C 2013, 117, 16076–16086

shifts are often attributed to an increased electrocatalytic activity of the electrode material. Here, however, the shift in the peak position is exclusively caused by the increase in electrode porosity.

A closer inspection of the CVs in Figure 7a reveals that at V = 37 nL not only a peak shift occurs but also a secondary peak emerges to the left of the original oxidation peak. With increasing pore volume, this peak increases in magnitude and eventually dominates the CV. In order to understand this observation, we again turn to numerical simulations (Figure 8). To mimic the transition seen in Figure 7a, we simulate CVs for various thicknesses of the porous electrodes in the range from 0 (flat electrode) to 20 μm ($V \approx 0.44$ μL). Similar to our experimental results, we find that with increasing layer thickness, i.e., with increasing cumulative pore volume, the oxidation peak shifts from an initial value of 577 mV to lower potentials until at a thickness of 10 μm the emergence of a second peak can be seen. This peak grows in magnitude as electrode thickness increases further and reaches a potential of 262 mV at the final electrode thickness of 20 μm.

While in the experiment we can only vary electrode thickness and thus V, the simulation offers the opportunity to also change the characteristic pore size. In Figure 8b, we plot the peak positions obtained with 20 μm thick electrodes of different pore sizes. We find that the peak potential becomes smaller as the pore size decreases. The changes of peak potential with varying electrode thickness and pore size are summarized in Figure 8c. The plot of peak potential versus electrode thickness shows qualitatively the same behavior as our experimental data presented in Figure 7b: An initial steep drop in E_{pp} with increasing electrode thickness is followed by a leveling of the curve.

Contrary to the case of a Nernstian system, in the case of irreversible dynamics, the redox reactions within the porous film and at the electrode/bulk electrolyte interface are strongly coupled through diffusion (Figure 8d). The reduced species is being oxidized so slowly that there is sufficient time to replenish the electrolyte solution within the porous film at most film thicknesses studied. As a consequence, in the case of small electrode thickness (up to ~5 μm), the entirety of the porous electrode takes part in the oxidation of the redox species, which diffuses into the electrode from the bulk electrolyte at the same rate with which it is oxidized within the porous film. The effect of the porosity is thus in this case primarily an increase of effective surface area. Only at film thicknesses at and above the diffusion length within the electrode $l = \sqrt{D_P \tau} \approx 14$ μm (for τ = 3 s, corresponding to the time needed to increase overpotential from 0 mV to past the oxidation peak for 20 μm electrode thickness), pore depletion becomes significant and gives rise to the formation of a thin-film diffusion-like peak at low potential. The location of this peak depends on the rate of pore depletion. Since smaller pores can be depleted more quickly than larger ones, the oxidation peak shifts to smaller potential (i.e., earlier time in the CV measurement) as the pore size is decreased (Figure 8c inset). For infinitesimally small r, the pore depletion peak will be centered around the standard potential of the electrochemical reaction, resembling reaction of an adsorbed redox species.[42] We should note that as we vary pore size in our simulations, we do not adjust for related changes in diffusivity of redox species and thus show the isolated effect of pore size only. In an experimental system that would allow for adjustment of r, a decrease in average pore size would certainly also hinder diffusive transport and thus potentially move the system from a regime where pores can be replenished (large pores) toward a pore depletion regime, where diffusive exchange of species between the bulk electrolyte and the porous film can be neglected.

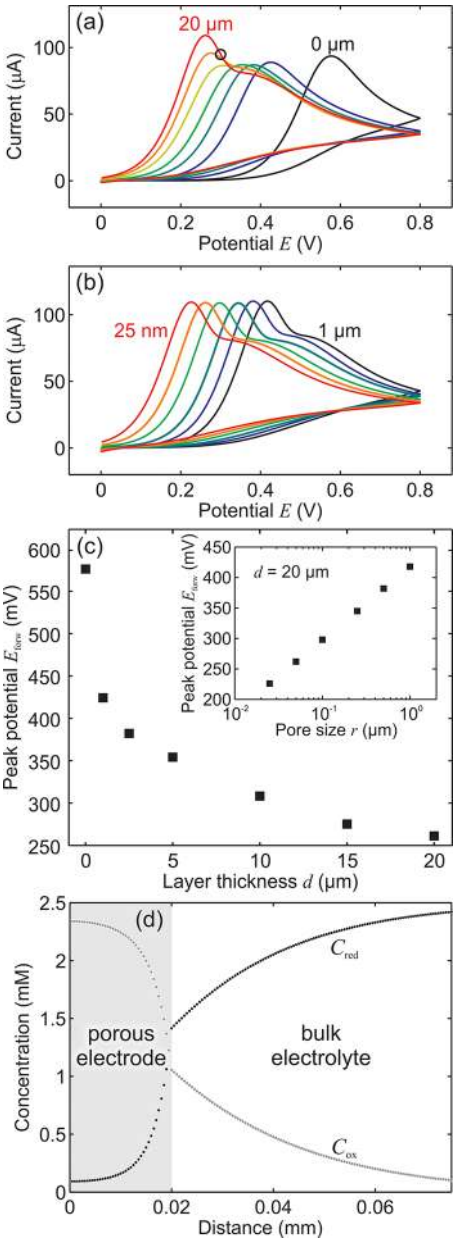

Figure 8. Numerical simulations for irreversible electrode kinetics: $k_0 = 10^{-7}$ cm/s, $E_0 = 0$ mV, and $A_0 = 0.22$ cm^2. (a) CVs generated for different thicknesses of the porous film of 0, 1, 2, 5, 10, 15, and 20 μm. (b) CVs generated for films with 20 μm thickness and characteristic pore sizes of 25, 50, 100, 250, 500, and 1000 nm. (c) Plots of peak potential as a function of thickness of the porous electrode (corresponding to simulations shown in panel a) and of the characteristic pore size (inset, corresponding to panel b). (d) Concentration profiles for reduced and oxidized species for a 20 μm thick electrode at 300 mV (black circle in panel a).

The effectiveness of a porous electrode can be characterized by a parameter that relates the reaction time scale to the diffusive transport time scale in the electrode film. We define this parameter as

dx.doi.org/10.1021/jp405142k | J. Phys. Chem. C 2013, 117, 16076−16086

$$\eta = \frac{rD_P}{d^2 k_0} \quad (4)$$

This dimensionless parameter is equivalent to the square of the Thiele modulus known in the context of porous catalysts in chemical engineering.[45] Values of $\eta < 1$ indicate that diffusive transport is too slow to supply the entire film with reactant, and therefore, the reactant is depleted within the majority of the electrode pore space. This is, for example, the case for the oxidation of FC at an electrode with $d = 20$ μm and $r = 80$ nm (resembling our experimental data), where $\eta < 10^{-5}$, and where the electrochemical response is dominated by pore depletion effects. However, $\eta > 1$ indicates that the reaction rate can be further improved by increasing the electrode thickness because the reactant can easily diffuse through the entire porous film and little reactant depletion occurs. For the oxidation of a redox species with $k_0 = 10^{-7}$ cm/s on a 20 μm thick electrode (Figure 8), η is on the order of 1, indicating that a large fraction of the accessible electrode surface within the porous film participates in the oxidation reaction, giving rise to an effective electrocatalytic behavior.

These considerations become particularly important if we no longer considered CVs but instead were to employ steady-state techniques such as chronoamperometry at a rotating disc electrode. Here, the reactant concentration at the electrode/bulk electrolyte interface is constant over time, and the measured redox current at a given potential depends solely on the number of available reaction sites and the reactant concentration.[42] Therefore, the appropriate value of d can be directly determined from eq 4. For irreversible reactions that tend to cause electrode fouling, such as the oxidation of NADH or other biomolecules, a porous electrode with $\eta > 1$ is beneficial: While those parts of the electrode that are located closest to the bulk electrolyte and thus initially experience the highest reaction rates become nonreactive due to fouling, diffusion through the porous electrode can transport the analyte to layers that lie beyond the fouled part of the film (assuming pore clogging does not occur), which increases the life of the electrode.

4. CONCLUSIONS

Our experimental results show that, using drop casting approaches, it is impossible to prepare electrodes from nanomaterials such as FGSs without introducing significant amounts of electrode porosity. For Nernstian and quasi-reversible systems, porosity-related effects such as decreased peak-to-peak separation and increased peak currents are observed even with some presumably flat ML electrodes. Without careful elimination of electrode porosity and roughness or use of extrapolation techniques as described above, only effective, i.e., morphology-related, reaction kinetics can be determined from CVs but not the intrinsic electrochemical kinetics of the electrode material. This is of significance for the comparison of the electroactivity of different electrode materials, which can be caused both by the morphological effects discussed here and by differences in intrinsic material properties such as functionalization or defectiveness.

For reversible and quasi-reversible systems, diffusive transport from the bulk electrolyte into the porous electrode film is negligible, and the thin-film diffusion response caused by pore depletion is (in good approximation) decoupled from the classical linear semi-infinite diffusion response at the electrode/bulk electrolyte interface. This can be used to determine pore volume and average pore size from experimental data through a mathematical separation of the thin-film diffusion-limited and the semi-infinite diffusion-limited redox currents that constitute the overall response.

In the case of irreversible redox reactions, porous electrodes show large peak shifts compared to flat electrodes. For electrode thicknesses up to the diffusion length within the porous film, these shifts are due to an increasing number of available reaction sites in the electrode, which are supplied with reactant through diffusion from the bulk electrolyte. In other words, electrode porosity effectively increases the reaction rate, and thus a morphology-related electrocatalytic effect is present.

AUTHOR INFORMATION

Corresponding Author

*(I.A.A.) E-mail: iaksay@princeton.edu.

Author Contributions

The manuscript was written through contributions of all authors. All authors have given approval to the final version of the manuscript.

Notes

The authors declare no competing financial interest.

ACKNOWLEDGMENTS

This work was supported by the Pacific Northwest National Laboratory (operated for the United States Department of Energy by Battelle) under grant number DE-AC05-76RL01830 and by the Small Business Innovation Research program of the National Science Foundation under grant number IIP-1142890.

REFERENCES

(1) Rolison, D. R. Catalytic Nanoarchitectures: the Importance of Nothing and the Unimportance of Periodicity. *Science* **2003**, *299*, 1698−1701.

(2) Newman, J.; Thomas-Alyea, K. E. *Electrochemical Systems*, 3rd ed.; Wiley: Hoboken, NJ, 2004.

(3) Newman, J.; Tiedemann, W. Porous-Electrode Theory with Battery Applications. *AIChE J.* **1975**, *21*, 25−41.

(4) Ogasawara, T.; Debart, A.; Holzapfel, M.; Novak, P.; Bruce, P. G. Rechargeable Li_2O_2 Electrode for Lithium Batteries. *J. Am. Chem. Soc.* **2006**, *128*, 1390−1393.

(5) Xiao, J.; Mei, D. H.; Li, X. L.; Xu, W.; Wang, D. Y.; Graff, G. L.; Bennett, W. D.; Nie, Z. M.; Saraf, L. V.; Aksay, I. A.; Liu, J.; Zhang, J. G. Hierarchically Porous Graphene as a Lithium-Air Battery Electrode. *Nano Lett.* **2011**, *11*, 5071−5078.

(6) Niedrach, L. W.; Alford, H. R. A New High-Performance Fuel Cell Employing Conducting-Porous-Teflon Electrodes and Liquid Electrolytes. *J. Electrochem. Soc.* **1965**, *112*, 117−124.

(7) Passalacqua, E.; Lufrano, F.; Squadrito, G.; Patti, A.; Giorgi, L. Nafion Content in the Catalyst Layer of Polymer Electrolyte Fuel Cells: Effects on Structure and Performance. *Electrochim. Acta* **2001**, *46*, 799−805.

(8) Menzel, N.; Ortel, E.; Kraehnert, R.; Strasser, P. Electrocatalysis Using Porous Nanostructured Materials. *ChemPhysChem* **2012**, *13*, 1385−1394.

(9) Oregan, B.; Gratzel, M. A Low-Cost, High-Efficiency Solar-Cell Based on Dye-Sensitized Colloidal TiO_2 Films. *Nature* **1991**, *353*, 737−740.

(10) Papageorgiou, N. Counter-Electrode Function in Nanocrystalline Photoelectrochemical Cell Configurations. *Coord. Chem. Rev.* **2004**, *248*, 1421−1446.

(11) Wang, Q.; Moser, J. E.; Gratzel, M. Electrochemical Impedance Spectroscopic Analysis of Dye-Sensitized Solar Cells. *J. Phys. Chem. B* **2005**, *109*, 14945−14953.

(12) Roy-Mayhew, J. D.; Bozym, D. J.; Punckt, C.; Aksay, I. A. Functionalized Graphene as a Catalytic Counter Electrode in Dye-Sensitized Solar Cells. *ACS Nano* **2010**, *4*, 6203−6211.
(13) Yuan, Z. Y.; Su, B. L. Insights into Hierarchically Meso-Macroporous Structured Materials. *J. Mater. Chem.* **2006**, *16*, 663−677.
(14) Lee, J.; Kim, J.; Hyeon, T. Recent Progress in the Synthesis of Porous Carbon Materials. *Adv. Mater.* **2006**, *18*, 2073−2094.
(15) Li, Y.; Fu, Z. Y.; Su, B. L. Hierarchically Structured Porous Materials for Energy Conversion and Storage. *Adv. Funct. Mater.* **2012**, *22*, 4634−4667.
(16) Newman, J. S.; Tobias, C. W. Theoretical Analysis of Current Distribution in Porous Electrodes. *J. Electrochem. Soc.* **1962**, *109*, 1183−1191.
(17) Biesheuvel, P. M.; Fu, Y. Q.; Bazant, M. Z. Diffuse Charge and Faradaic Reactions in Porous Electrodes. *Phys. Rev. E* **2011**, *83*, 061507.
(18) Ferguson, T. R.; Bazant, M. Z. Nonequilibrium Thermodynamics of Porous Electrodes. *J. Electrochem. Soc.* **2012**, *159*, A1967−A1985.
(19) Wang, J. Carbon-Nanotube Based Electrochemical Biosensors: A Review. *Electroanalysis* **2005**, *17*, 7−14.
(20) Gooding, J. J. Nanostructuring Electrodes with Carbon Nanotubes: A Review on Electrochemistry and Applications for Sensing. *Electrochim. Acta* **2005**, *50*, 3049−3060.
(21) Pumera, M. The Electrochemistry of Carbon Nanotubes: Fundamentals and Applications. *Chem.—Eur. J.* **2009**, *15*, 4970−4978.
(22) Shao, Y. Y.; Wang, J.; Wu, H.; Liu, J.; Aksay, I. A.; Lin, Y. H. Graphene Based Electrochemical Sensors and Biosensors: A Review. *Electroanalysis* **2010**, *22*, 1027−1036.
(23) Pumera, M. Graphene-Based Nanomaterials and Their Electrochemistry. *Chem. Soc. Rev.* **2010**, *39*, 4146−4157.
(24) Zhu, Z. G.; Garcia-Gancedo, L.; Flewitt, A. J.; Xie, H. Q.; Moussy, F.; Milne, W. I. A Critical Review of Glucose Biosensors Based on Carbon Nanomaterials: Carbon Nanotubes and Graphene. *Sensors* **2012**, *12*, 5996−6022.
(25) Zhou, M.; Zhai, Y. M.; Dong, S. J. Electrochemical Sensing and Biosensing Platform Based on Chemically Reduced Graphene Oxide. *Anal. Chem.* **2009**, *81*, 5603−5613.
(26) Moore, R. R.; Banks, C. E.; Compton, R. G. Basal Plane Pyrolytic Graphite Modified Electrodes: Comparison of Carbon Nanotubes and Graphite Powder as Electrocatalysts. *Anal. Chem.* **2004**, *76*, 2677−2682.
(27) Stankovich, S.; Dikin, D. A.; Piner, R. D.; Kohlhaas, K. A.; Kleinhammes, A.; Jia, Y.; Wu, Y.; Nguyen, S. T.; Ruoff, R. S. Synthesis of Graphene-Based Nanosheets Via Chemical Reduction of Exfoliated Graphite Oxide. *Carbon* **2007**, *45*, 1558−1565.
(28) Schniepp, H. C.; Li, J. L.; McAllister, M. J.; Sai, H.; Herrera-Alonso, M.; Adamson, D. H.; Prud'homme, R. K.; Car, R.; Saville, D. A.; Aksay, I. A. Functionalized Single Graphene Sheets Derived from Splitting Graphite Oxide. *J. Phys. Chem. B* **2006**, *110*, 8535−8539.
(29) McAllister, M. J.; Li, J. L.; Adamson, D. H.; Schniepp, H. C.; Abdala, A. A.; Liu, J.; Herrera-Alonso, M.; Milius, D. L.; Car, R.; Prud'homme, R. K.; Aksay, I. A. Single Sheet Functionalized Graphene by Oxidation and Thermal Expansion of Graphite. *Chem. Mater.* **2007**, *19*, 4396−4404.
(30) Kudin, K. N.; Ozbas, B.; Schniepp, H. C.; Prud'homme, R. K.; Aksay, I. A.; Car, R. Raman Spectra of Graphite Oxide and Functionalized Graphene Sheets. *Nano Lett.* **2008**, *8*, 36−41.
(31) Kang, X. H.; Wang, J.; Wu, H.; Liu, J.; Aksay, I. A.; Lin, Y. H. A Graphene-Based Electrochemical Sensor for Sensitive Detection of Paracetamol. *Talanta* **2009**, *81*, 754−759.
(32) Kang, X. H.; Wang, J.; Wu, H.; Aksay, I. A.; Liu, J.; Lin, Y. H. Glucose Oxidase-Graphene-Chitosan Modified Electrode for Direct Electrochemistry and Glucose Sensing. *Biosens. Bioelectron.* **2009**, *25*, 901−905.
(33) Punckt, C.; Pope, M. A.; Liu, J.; Lin, Y. H.; Aksay, I. A. Electrochemical Performance of Graphene as Effected by Electrode Porosity and Graphene Functionalization. *Electroanalysis* **2010**, *22*, 2834−2841.
(34) Roy-Mayhew, J. D.; Boschloo, G.; Hagfeldt, A.; Aksay, I. A. Functionalized Graphene Sheets as a Versatile Replacement for Platinum in Dye-Sensitized Solar Cells. *ACS Appl. Mater. Interfaces* **2012**, *4*, 2794−2800.
(35) Zuo, X. B.; Xu, C. S.; Xin, H. W. Simulation of Voltammogram on Rough Electrode. *Electrochim. Acta* **1997**, *42*, 2555−2558.
(36) Menshykau, D.; Compton, R. G. The Influence of Electrode Porosity on Diffusional Cyclic Voltammetry. *Electroanalysis* **2008**, *20*, 2387−2394.
(37) Menshykau, D.; Streeter, I.; Compton, R. G. Influence of Electrode Roughness on Cyclic Voltammetry. *J. Phys. Chem. C* **2008**, *112*, 14428−14438.
(38) Streeter, I.; Wildgoose, G. G.; Shao, L. D.; Compton, R. G. Cyclic Voltammetry on Electrode Surfaces Covered with Porous Layers: An Analysis of Electron Transfer Kinetics at Single-Walled Carbon Nanotube Modified Electrodes. *Sens. Actuators, B* **2008**, *133*, 462−466.
(39) Keeley, G. P.; Lyons, M. E. G. The Effects of Thin Layer Diffusion at Glassy Carbon Electrodes Modified with Porous Films of Single-Walled Carbon Nanotubes. *Int. J. Electrochem. Sci* **2009**, *4*, 794−809.
(40) Pope, M. A.; Punckt, C.; Aksay, I. A. Intrinsic Capacitance and Redox Activity of Functionalized Graphene Sheets. *J. Phys. Chem. C* **2011**, *115*, 20326−20334.
(41) Marcano, D. C.; Kosynkin, D. V.; Berlin, J. M.; Sinitskii, A.; Sun, Z. Z.; Slesarev, A.; Alemany, L. B.; Lu, W.; Tour, J. M. Improved Synthesis of Graphene Oxide. *ACS Nano* **2010**, *4*, 4806−4814.
(42) Bard, J. A.; Faulkner, L. R. *Electrochemical Methods*, 2nd ed.; John Wiley & Sons: New York, 2001.
(43) Albaalbaki, B.; Hill, R. J. On Molecular Diffusion in Nanostructured Porous Media: Interfacial Exchange Kinetics and Surface Diffusion. *Proc. R. Soc. A* **2012**, *468*, 3100−3120.
(44) Bonilla, M. R.; Bhatia, S. K. Diffusion in Pore Networks: Effective Self-Diffusivity and the Concept of Tortuosity. *J. Phys. Chem. C* **2012**, *117*, 3343−3357.
(45) Fogler, H. S. *Elements of Chemical Reaction Engineering*; Prentice Hall PTR: Upper Saddle River, NJ, 2002.
(46) Adler, S. B.; Lane, J. A.; Steele, B. C. H. Electrode Kinetics of Porous Mixed-Conducting Oxygen Electrodes. *J. Electrochem. Soc.* **1996**, *143*, 3554−3564.
(47) Compton, R. G.; Banks, C. R. *Understanding Voltammetry*, 2nd ed.; World Scientific: Singapore, 2010.
(48) de Levie, R. On Porous Electrodes in Electrolyte Solutions. *Electrochim. Acta* **1963**, *8*, 751−780.